Journal of Materials Chemistry A

PAPER

View Article Online
View Journal | View Issue

Cite this: J. Mater. Chem. A, 2017, 5, 17312

Hierarchical $CoMoO_4$@Co_3O_4 nanocomposites on an ordered macro-porous electrode plate as a multi-dimensional electrode in high-performance supercapacitors†

Mai Li, *[a] Yuanhao Wang,[b] Hongxing Yang[a] and Paul K. Chu[c]

Nanoscale core–shell $CoMoO_4$@Co_3O_4 composite materials are fabricated by a multi-step hydrothermal process on the surface and side wall of an ordered macro-porous electrode plate (OMEP) as the active electrode in a high power density storage device. The morphology, formation mechanism of the $CoMoO_4$@Co_3O_4 nanostructure, and capacitor performance are systematically studied. The $CoMoO_4$@Co_3O_4/OMEP electrode has a capacity of 7.13 F cm^{-2} (1168.0 F g^{-1}) at a constant current density of 0.6 A g^{-1} and a retention ratio of 81.4% after 5000 cycles. The large specific capacitance and excellent rate capability can be attributed to the unique 3D ordered porous architecture which facilitates electron and ion transport, enlarges the liquid–solid interfacial area, prevents agglomeration of nanomaterials, and boosts the utilization efficiency of the active materials. Reconstruction on the surface of the porous structured substrate enhances the power density and cycling performance at large current densities. Using the $CoMoO_4$@Co_3O_4/OMEP electrode as the positive electrode and active carbon/nickel foam (AC/NF) as the negative electrode, the electrochemical electrode packaged in a CR2025 battery cell as a miniature hybrid device exhibits stable power characteristics (10 000 cycles with 91.7% retention at a current of 0.1 A). The device produces large instantaneous power that charging it for 10 s and using three devices in series can power four parallel LED arrays at a current of 0.152 A.

Received 8th June 2017
Accepted 19th July 2017

DOI: 10.1039/c7ta04981a

rsc.li/materials-a

1. Introduction

Growing fossil fuel consumption and related environmental concerns have sparked intensive research on sustainable energy production and conversion systems with low cost, high efficiency, and environmental benignity with low CO_2 emission.[1] Supercapacitors, as one of the most important energy storage devices, are viable energy storage devices for high power supplies as well as electric and hybrid vehicles due to the high power density, fast charging–discharging rates, and long cycle life.[2] Supercapacitors also bridge the power/energy gap between solar cells/batteries/fuel cells and conventional electrostatic capacitors. According to the charge storage mechanisms, supercapacitors can be classified as electrical double-layer capacitors (EDLCs) and pseudocapacitors (PCs).[3] In particular, PCs based on the fast reversible faradic redox reactions as well as ion adsorption and desorption like EDLCs on the electrode surface usually provide larger specific capacitance than supercapacitors composed of carbonaceous materials based on electric double-layer charge storage.[4–6] Therefore, current research has focused on PCs and the specific capacitance of some transition metal oxides, hydroxide-based pseudocapacitive materials or combinations of them such as MnO_2,[7] V_2O_5,[8] Fe_2O_3,[9] Co_3O_4,[10] CoO[10] and NiO[11] because of the relative low cost, manufacturability, and flexibility.

Among the various metal oxides, Co_3O_4 has attracted much interest because of its high theoretical specific capacitance, good redox performance, easily controllable size or shape, and tunable structural identities.[12–14] Rakhi[15] prepared mesoporous cobalt oxide nanosheets electrode arrays on flexible carbon paper substrates using an economical and scalable two-step process and the Co_3O_4 nanosheets delivered a high specific capacitance of 905.0 F g^{-1} even at a current density of 1 A g^{-1}. However, due to the poor electrical conductivity and volume changes during cycling, the Co_3O_4 electrode usually suffers from poor rate capability and rapid capacity fading, resulting in unsatisfactory cycling performance. Furthermore, the spontaneous aggregation of Co_3O_4 materials is effectively unsolved,[16,17] which prevents their further application such as

[a]Renewable Energy Research Group, Department of Building Services Engineering, The Hong Kong Polytechnic University, Hung Hom, Kowloon, Hong Kong, China. E-mail: mai.li@polyu.edu.hk; Fax: +852 2766 7198; Tel: +852 5606 5568

[b]Faculty of Science and Technology, Technological and Higher Education Institute of Hong Kong, New Territories, Hong Kong, China

[c]Department of Physics and Materials Science, City University of Hong Kong, Tat Chee Avenue, Kowloon, Hong Kong, China

† Electronic supplementary information (ESI) available. See DOI: 10.1039/c7ta04981a

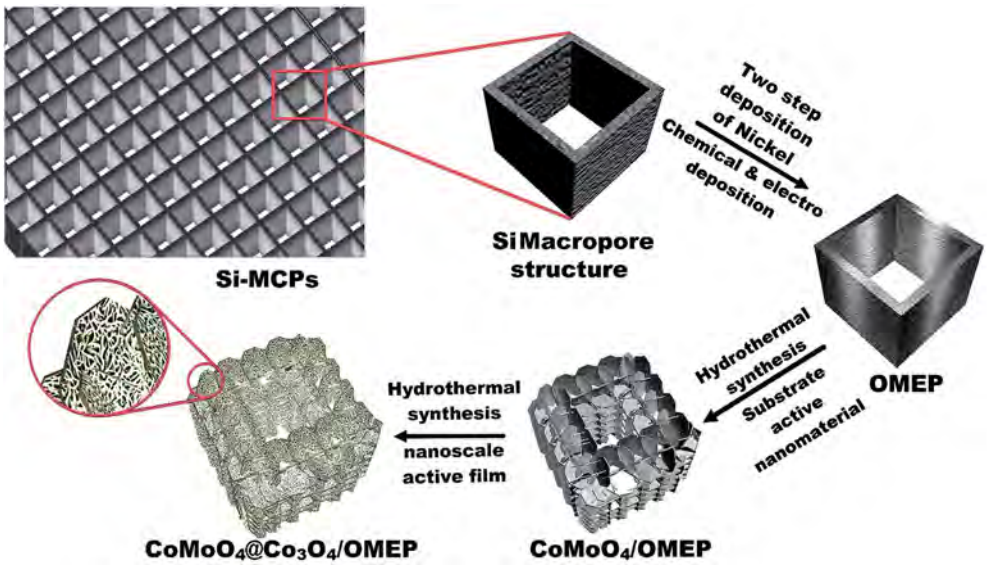

Fig. 1 Illustration of the procedures to prepare the $CoMoO_4@Co_3O_4$/OMPE multi-dimensional nanocomposite.

supercapacitors,[18] heterogeneous catalysts,[19] electrochemical sensors,[19] and lithium storage.[20] Hence, the performance must be improved by developing functional nanocomposite materials with synergistic effects and much effort has been devoted to combining the unique properties of individual constituents to improve the electrochemical performance,[12,21–23] for instance, composite structures like $Co_3O_4@NiMoO_4$,[3] $NiCo_2O_4@NiMoO_4$,[24] $Ni(OH)_2@CoMoO_4$,[25] $NiCo_2S_4@Co(OH)_2$ [26] and $NiCo_2O@MnMoO_4$.[27] Those three-dimensional (3D) hierarchical composites exhibit excellent structural advantages such as the large surface area, strong permeability, and ample surface active sites. Using a reflux technique, Mai *et al.*[22] synthesized 3D hierarchical $MnMoO_4/CoMoO_4$ heterostructured nanowires with enhanced supercapacitor performance and larger specific capacitance than the single components of either $MnMoO_4$ or $CoMoO_4$.[22] Huang *et al.*[24] fabricated hierarchical core–shell $NiCo_2O_4@NiMoO_4$ nanowires on carbon cloth ($CC@NiCo_2O_4@NiMoO_4$) by a two-step hydrothermal technique for flexible binder-free electrodes with a larger areal capacitance of 2.917 F cm^{-2} at 2 mA cm^{-2} and 90.6% retention for 2000 cycles at a large current density of 20 mA cm^{-2}.

Herein, we describe a two-step hydrothermal strategy to prepare 3D hierarchical $CoMoO_4@Co_3O_4$ composite films on a 3D ordered macro-porous electrode plate (OMEP) as a high-performance multidimensional faradaic electrode. The advantage of a porous structure is summarized for battery performance,[28] but few similar research studies exist on ordered porous materials like OMEPs in the field of supercapacitors. OMEPs with a typical pore size of 5 μm and channel depth of 270 μm can be produced by standard silicon and nanoscale technology.[29] The $CoMoO_4$ nanoflakes are chosen for pseudocapacitive and electrocatalytic reasons arising from the large cell parameters ($a = 10.21$ A, $b = 9.268$ A, $c = 7.022$ A) with stable electrochemical properties.[30] The inner wall of the OMEP provides the space needed for the nickel current collector layer and $CoMoO_4@Co_3O_4$ composite active materials and so the footprint of the electrode can be reduced while maintaining the advantage of a large surface area as shown in Fig. 1. $CoMoO_4$ is first deposited onto the radically ordered OMEP to form the $CoMoO_4$/OMEP hierarchical 3D nanostructure by hydrothermal self-assembly and then a nanocomposite layer of the Co_3O_4 nanostructure is prepared on the surface of $CoMoO_4$/OMEP to fabricate the multi-dimensional electrode. The multi-dimensional hybrid nanostructure boasting a large surface area and short diffusion path for electrons and ions reduces agglomeration of materials.

2. Experimental details

2.1 Materials

The chemical reagents such as nickel chloride $\{NiCl_2 \cdot 6H_2O\}$, sodium hypophosphite monohydrate $\{NaH_2PO_2 \cdot H_2O\}$, ammonium chloride $\{NH_4Cl\}$, ammonium $\{NH_3 \cdot H_2O\}$, chloride hexahydrate $\{CoCl_2 \cdot 6H_2O\}$, nickel acetate tetrahydrate $\{C_4H_6O_4Ni \cdot 4H_2O\}$ and ammonium molybdate tetrahydrate $\{(NH_4)_6Mo_7O_{24} \cdot 4H_2O\}$ were of analytical reagent grade and used as received without further purification. The aqueous solutions were prepared with 18 MΩ deionized water and all the experiments were carried out at room temperature.

2.2 Fabrication of low-resistance ordered macro-porous electrode plate

The liquid flow plating method from Wang *et al.*[31,32] was used to chemical deposition a nickel layer on both the outer surface and inner side wall of the silicon macrochannel plate[33] (Si-MCP, as illustrated in Fig. 2(a)) to fabricated the ordered macro-porous electrode plate (OMEP). Fig. S1† shows the schematic diagram of the device and working principle for liquid flow deposition of a nickel layer on the surface and side wall of Si-MCP.[32] Under the action of gravity and a water pump, the deposition fluid

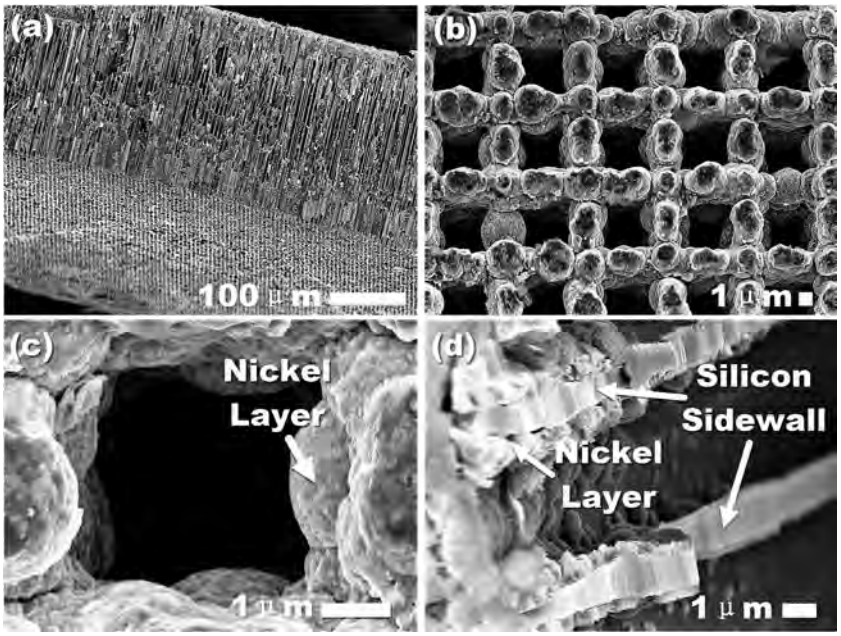

Fig. 2 SEM images: (a) top surface of the ordered Si-MCPs; (b) top surface of nano-Ni covered OMEP; (c) close-range details of nano-Ni particles in a pore; (d) cross-sectional view of the nano-Ni covered OMEP.

flows continuously through the surface and interior of the Si-MCP and the OMEP with a dense and uniform nickel layer was obtained. As shown in Fig. S2(a),† in nickel plating carried out by a conventional method, the amount of the nickel inside the Si-MCP is very limited, whereas, from Fig. S2(b),† it is seen that in the conducive layer fabricated through the liquid flow deposition method, the nickel on the channel of the OMEP is very dense which reduces the internal resistance and improves the life and performance of the device significantly. In order to improve the surface area and conductivity of the OMEP, porous nano-Ni shown in Fig. 2(b)–(d) was created by the electrochemical nickel plating method performed in a standard two electrode glass cell at 23 ± 1 °C in an electrolyte consisting of 2 M NH_4Cl and 0.1 M $NiCl_2$ at a pH of 3.5 with the clean OMEP as the working electrode and Pt foil as the counter electrode. The distance between the two electrodes was 1 cm and electrodeposition was carried out at a constant current of 0.25 A cm^{-2} for 90 s.

2.3 Synthesis of the hierarchical multidimensional $CoMoO_4$@Co_3O_4/OMEP composite

$CoMoO_4$ was prepared hydrothermally. The macroporous electrically conductive network (OMEP) was cut into small thin foils with an area of 0.8 × 0.9 cm^2, put into a buffer solution of Triton X-100 for at least 2 minutes to increase the hydrophilicity, and placed standing against the wall of a Teflon-lined stainless steel autoclave. The reaction solution was obtained by mixing 2 mmol $CoCl_2 \cdot 6H_2O$, 2 mmol $(NH_4)_6Mo_7O_{24} \cdot 4H_2O$, 5 mmol NH_4F, and 5 mmol of urea in 100 mL of distilled water under magnetic stirring and transferred to the Teflon-lined autoclave. The reaction proceeded for 2.5 h at a temperature of 120 °C, resulting in the formation of a violet precipitate on the surface of the OMEP. The coated OMEP was cleaned by deionized water and ethanol to remove the impurities in the surface, and then dried in an oven at 80 °C for 12 h. Finally, the sample was annealed in a pure Ar atmosphere at 300 °C for 2 h to obtain $CoMoO_4$/OMEP.

Co_3O_4 was prepared by a hydrothermal method. The cleaned $CoMoO_4$/OMEP was placed standing against the wall of a Teflon-lined stainless steel autoclave. The reaction solution was obtained by mixing 1 mmol $CoCl_2 \cdot 6H_2O$, 10 mmol NH_4F, and 10 mmol urea in 100 mL of distilled water under magnetic stirring and transferred into the Teflon-lined autoclave liner. After reacting for 1.5 h at 140 °C, the OMEP with the as-grown hydrate precursors was dried at 80 °C for 2 h and annealed at 300 °C for 2 h in Ar to obtain the $CoMoO_4$@Co_3O_4/OMEP. In order to study the performance of the device with a planar structure, $CoMoO_4$@Co_3O_4 was prepared on a Ni-covered silicon wafer for comparison. The fabrication steps and size of $CoMoO_4$@Co_3O_4/Ni/Si was the same as those of $CoMoO_4$@Co_3O_4/OMEP.

2.4 Characterization and fabrication of the asymmetrical device

The morphology and microstructure of the OMEP, Co_3O_4, $CoMoO_4$ and $CoMoO_4$@Co_3O_4 thin films were examined by field-emission scanning electron microscopy (FE-SEM, JEOL JSM-7001F, Japan) and the crystal structure was determined by X-ray diffraction (XRD, Rigaku, RINT2000, Japan). The Raman scattering spectra were recorded from 200 to 2000 cm^{-1} on an Olympus BX41 Raman Microprobe using a 524.5 nm argon ion laser. The elemental composition was determined by X-ray photoelectron spectroscopy (XPS, Kratos AXIS Ultra DLD). The TEM image, SAED patterns, lattice structure and EDS maps were

obtained by high-resolution transmission electron microscopy (STEM, Jeol JEM-2100F).

The electrochemical measurements were performed on a three-electrode electrochemical working station (Shanghai Chenhua CHI660D) with the saturated calomel electrode and platinum gauze electrode serving as the reference electrode and counter electrode, respectively. The measurements were conducted at room temperature in a 2 M KOH aqueous electrolyte. In order to determine the electrochemical properties and specific capacity of the electrode samples, CV scans were acquired from 0 to 0.45 V (*vs.* SCE) from each sample at different scanning rates. Chronopotentiometry tests were conducted in the potential range between 0 and 0.45 V at different constant current densities. The measurements of asymmetric pseudocapacitance (ASC) were carried out to estimate the practical value of the composite materials according to the CV scans from 0 to 1.5 V, charging–discharging tests from 0 to 1.5 V, as well as application tests. Impedance spectra were acquired from $CoMoO_4$@Co_3O_4/OMEP and ASC before and after the cycling test from 0.01 to 10 000 Hz to investigate the reaction mechanism of the electrode and device.

The asymmetrical device was assembled using the $CoMoO_4$@Co_3O_4/OMEP and active carbon/Ni-foam electrodes separated by a polyethylene (PE) membrane. The PE membrane was pretreated and dipped in KOH for 10 min and assembled with the electrodes in a CR2032 battery case with the quasi solid electrolyte. The specific capacitance (C_s), areal capacitance (C_a), specific capacitance from CV curves (C_{cv}), energy density (E), and power density (P) were calculated from the following equations:[34,35]

$$C_s = \frac{I \times \Delta t}{m \times \Delta V}, \quad (1)$$

$$C_a = \frac{I \times \Delta t}{S \times \Delta V}, \quad (2)$$

$$C_{cv} = \int i\mathrm{d}V/(s \times m \times \Delta V), \quad (3)$$

$$E = \frac{C(\Delta V)^2}{2}, \quad (4)$$

and

$$P = \frac{E}{\Delta t}, \quad (5)$$

Where I (A) is the current during the discharge process, Δt (s) is the discharge time, m (g) is the mass of the electroactive materials, ΔV (V) is the applied potential window, S (cm^2) is the area of the working electrode, $\int i\mathrm{d}V$ is the covered area of CV, and s ($mV\ s^{-1}$) is the scanning rate of CV.

3. Results and discussion

The rough morphology and excellent electrical conductivity of the OMEP can benefit the growth of nanomaterial transport of electrolyte ions and electrons and therefore two-step deposition of nano-scale Ni was conducted on the surface and sidewall of Si-MCP (Fig. 2(a)) as a key step.[36] After fabrication of the OMEP, a two-step hydrothermal method is employed to synthesize the active materials at a high temperature and pressure, so that the solution can easily penetrate the nanoscale electrode substrate and the hierarchical $CoMoO_4$@Co_3O_4 composite structure is prepared uniformly on the surface and sidewall of the 3D OMEP. The thin Co_3O_4, $CoMoO_4$, and $CoMoO_4$@Co_3O_4 films are deposited on the nickel-coated OMEP for comparison as shown in Fig. S3† and the electrochemical properties and effects of the solvents on the morphology of those samples are determined from an active area of 0.6 cm^2. The $CoMoO_4$@Co_3O_4 composite is prepared on a 0.6 cm^2 nickel covered silicon wafer by the same fabrication process and tested under the same conditions for comparison. Moreover, the asymmetric pseudocapacitor (ASC) is prepared to estimate the practical value of the composite materials.

3.1 Materials characterization

Fig. 2(a) depicts the SEM images of the Si-MCP providing a general view of the morphology of the sample showing a uniform structure. As shown in Fig. 2(b) and (c), OMEP retains not only the original 3D morphology, but also the nickel current collector with good uniformity and Fig. 2(d) reveals the uniform nickel layer on the side wall and interior of the OMEP. The structure of the nanoscale composite films is determined by X-ray diffraction as shown in Fig. 3(a). The XRD pattern of the backbone material OMEP without the deposited nanostructure is displayed and compared to that of Co_3O_4/OMEP and $CoMoO_4$@Co_3O_4/OMEP, it shows a stronger diffraction peaks of Ni (Ni: JCPDS card no. 01-089-7128) and Si, suggesting successful deposition of active materials on the substrate. The hierarchical $CoMoO_4$ nanostructure ($CoMoO_4$: JCPDS card no. 00-021-0868) and Co_3O_4 (Co_3O_4: JCPDS card no. 74-2120) in $CoMoO_4$@Co_3O_4/OMEP are shown in Fig. 3(a).[35] Fig. 3(b) shows the Raman scattering spectrum of the $CoMoO_4$@Co_3O_4/OMEP composite. Fig. 3(b) depicts the Raman spectra of the $CoMoO_4$ particles showing peaks at 335, 817, 880, and 936 cm^{-1} and other peaks at 478 and 521 cm^{-1} arising from the Co_3O_4 crystalline phase.[37,38] The valence states of oxygen, molybdenum and cobalt in $CoMoO_4$@Co_3O_4/OMEP are determined by XPS. The survey spectrum in Fig. 3(c) shows the presence of C, O, Ni, Co, Mo and Si being consistent with XRD [Fig. 3(a)] and EDS [Fig. S4†]. As shown in Fig. 3(d), the binding energies of the Co $2p_{3/2}$ and Co $2p_{1/2}$ photoelectrons are 779.8, 780.3, and 781.1 eV corresponding to Co_3O_4, CoOOH and $CoMoO_4$, respectively. The Mo 3d core-level spin–orbit doublets (at 232 and 235 eV) in Fig. 3(e) are in accordance with the reported value of a splitting width of 3.0 eV.[39,40] The Mo^{6+} peak is attributed to surface Mo species that have been oxidized upon air exposure. The O 1s spectrum shows five oxygen peaks, O1 (529.7 eV), O2 (530.0 eV), O3 (530.7 eV), O4 (531.9 eV), and O5 (532.7) ascribed to Co–OH, Co–O, Mo–O, Si–O and physisorbed/chemisorbed oxygen at/near the surface,[41,42] respectively, being consistent with the elemental valence states.

The morphology of the $CoMoO_4$ nanoflakes, Co_3O_4 nanosheets and $CoMoO_4$@Co_3O_4 nanocomposite on the OMEP is shown in Fig. 4(a)–(k). The $CoMoO_4$ nanoflakes on the Ni

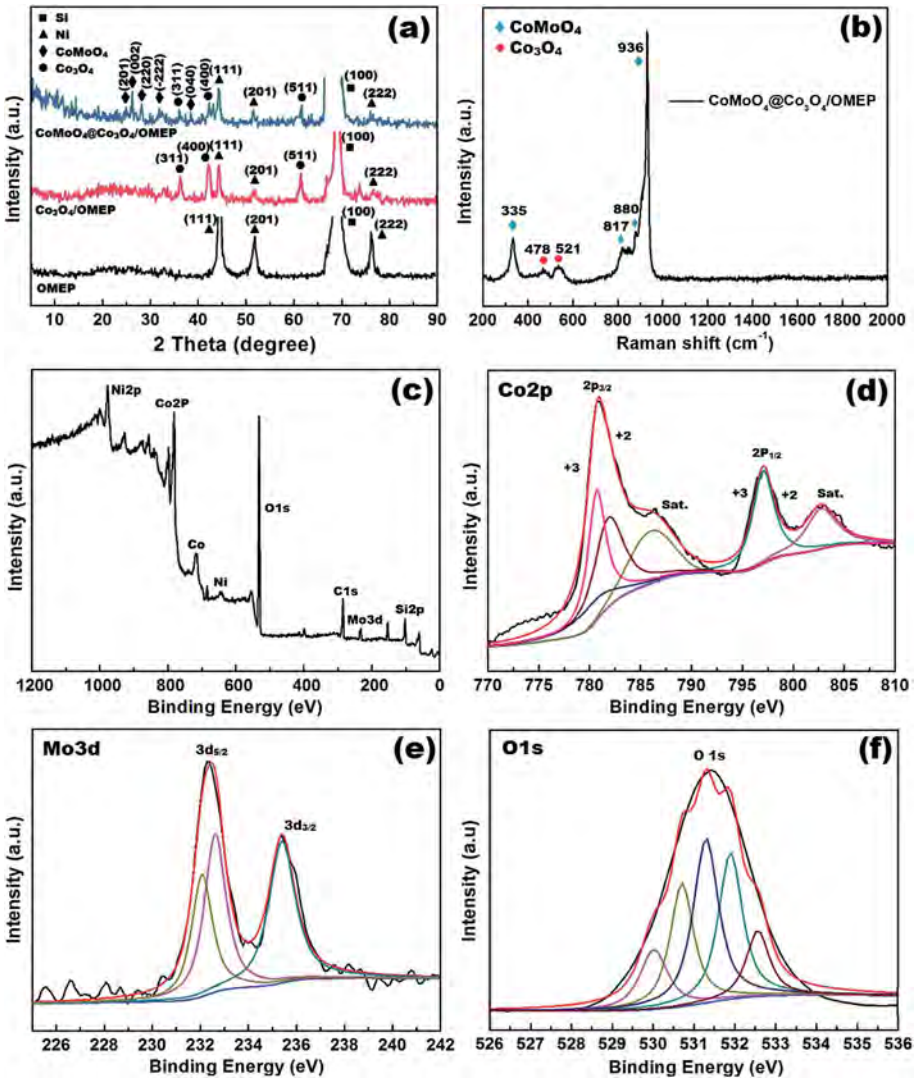

Fig. 3 (a) XRD patterns of $CoMoO_4$@Co_3O_4/OMEP, Co_3O_4/OMEP, and OMEP; (b) Raman scattering spectra of $CoMoO_4$@Co_3O_4/OMEP; (c) XPS survey spectrum of $CoMoO_4$@Co_3O_4/OMEP; XPS spectra of (d) Co 2p, (e) Mo 3d, and (f) O 1s for $CoMoO_4$@Co_3O_4/OMEP.

support layer are interconnected with each other forming a nanoscale bifunctional layer with an open network as shown in Fig. 4(a) and (b). As a result, most of the nanoflakes are readily accessible by the electrolyte when used as the faradaic electrode as well as physical support for the Co_3O_4 nanosheets. By controlling the hydrothermal reaction conditions, ultrathin Co_3O_4 nanosheets are obtained on the surface and sidewall of the OMEP as well as $CoMoO_4$ nanoflakes. As shown in Fig. 4(c) and (d), the Co_3O_4 nanosheets have an ultrathin structure with a typical thickness of 5 nm and so they can easily spread to the surface of other materials. Fig. 4(e) shows that the $CoMoO_4$@-Co_3O_4 on the surface of the OMEP increases the area and amount of active materials per unit area. Fig. 4(f) and (g) display the enlarged SEM image of a local area in Fig. 4(e) revealing ultrathin Co_3O_4 nanosheets on the surface and in the gap among the $CoMoO_4$ nanoflakes, which promote transport of electrons and space utilization. Owing to the ordered porous structure of the OMEP, the area of the inner wall is relatively large and Fig. 4(i) and (j) show that the $CoMoO_4$ nanoflakes and Co_3O_4 nanosheets have a morphology similar to that on the surface. The self-supporting multidimensional structure has higher space utilization than conductive layers like copper and aluminum foils and provides 3D paths for ions. Fig. 4(k) and (l) show that the nanostructured $CoMoO_4$@Co_3O_4 has a reticulate transfixion structure that promotes the interaction between electrons from the conduction layer and ions adsorbed on the surface of the nanomaterials from the electrolyte. The $CoMoO_4$@Co_3O_4 nanostructure is uniformly deposited on the sidewall of the macroporous, while maintaining the ion transport space in the channel to improve space utilization of the substrate electrode of the OMEP.

Transmission electron microscopy (TEM) is carried out to investigate the structure of the $CoMoO_4$, Co_3O_4, and $CoMoO_4$@Co_3O_4. Fig. 5(a) depicts the typical TEM image of lamellar $CoMoO_4$ after ultrasonic treatment in ethanol. The selected-area electron diffraction (SAED) patterns of the

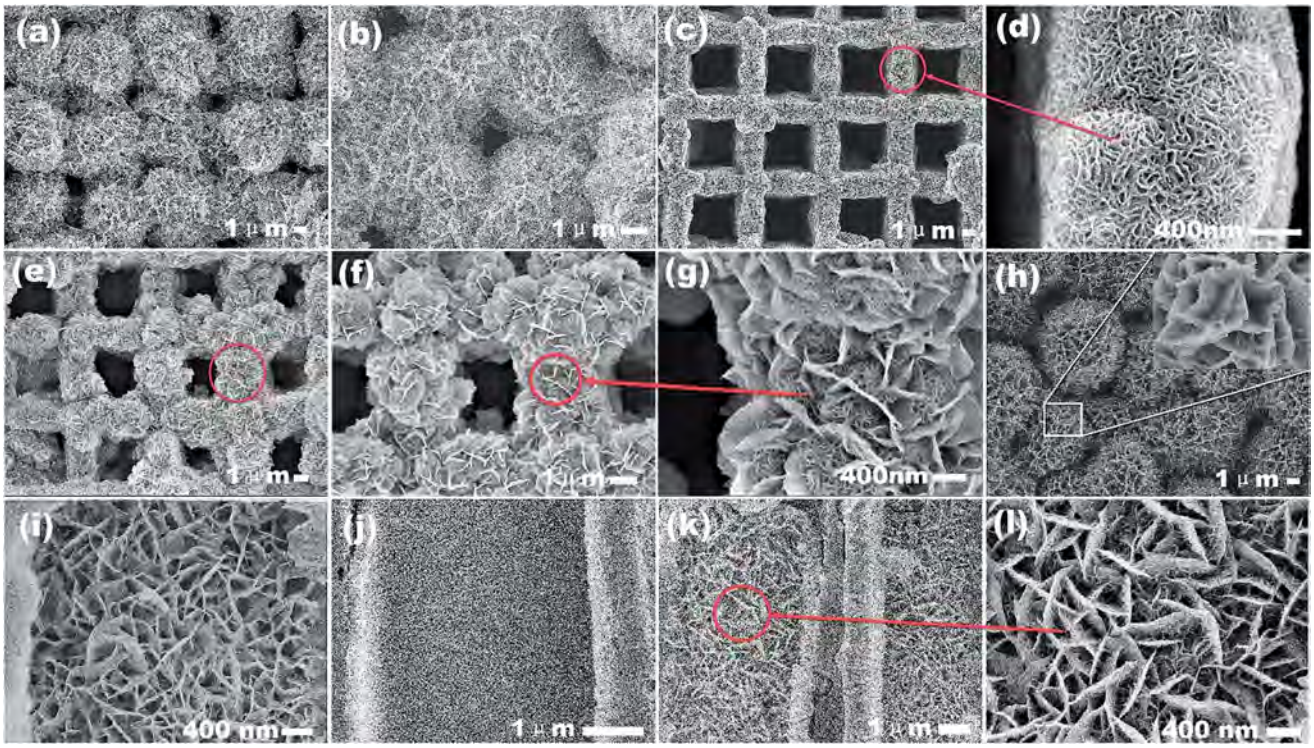

Fig. 4 SEM images of the $CoMoO_4$/OMEP structure: (a) top-view and (b) partial magnification of a single micro-porous from (a) Co_3O_4/OMEP: (c) top-view and (d) partial magnification of Co_3O_4 nanosheets from (c) the $CoMoO_4$@Co_3O_4/OMEP composite structure: (e) top-view and (f) partial magnification of a single micro-porous from (e) and (g) partial magnified view of (f) (h) $CoMoO_4$@Co_3O_4 on nickel covered silicon; SEM images of the cross-sectional view of the nanostructure on the side wall of the OMEP: (i) $CoMoO_4$ nanoflake and (j) Co_3O_4 nanosheets and (k) $CoMoO_4$@Co_3O_4 on the side wall of OMEP; (l) partial magnified view of (k).

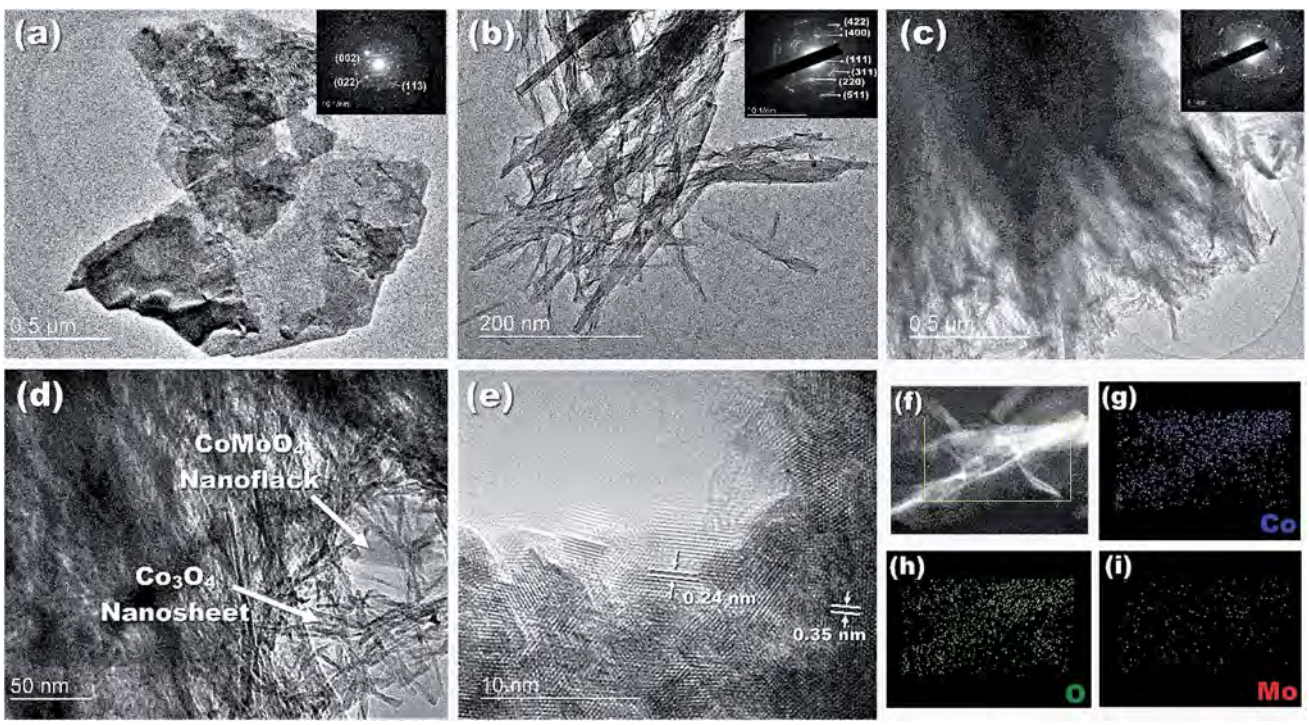

Fig. 5 (a–c) TEM images and SAED patterns of individual $CoMoO_4$ nanoflakes, Co_3O_4 nanosheets and the $CoMoO_4$@Co_3O_4 core–shell composite nanostructure; (d) magnified view of (c) (e) HR-TEM image of $CoMoO_4$@Co_3O_4; (f–i) EDS maps of $CoMoO_4$@Co_3O_4.

representative $CoMoO_4$ nanoflakes are shown in the inset of Fig. 5(a). Fig. 5(b) presents the typical TEM image and the selected-area electron diffraction (SAED) patterns of the representative Co_3O_4 nanosheets.[43] After the ultrasonic treatment in ethanol, the Co_3O_4 nanosheets spread out and their lamellar structure and lattice characteristics can be clearly observed. $CoMoO_4$ and Co_3O_4 have the same morphology consistent with that conveyed by SEM. The representative TEM and HR-TEM images of the precursor of $CoMoO_4@Co_3O_4$ are displayed in Fig. 5(c)–(e) and the inset. The precursor $CoMoO_4$ is coated with Co_3O_4 to form a stacked core–shell heterostructure (Fig. 5(c)) and HR-TEM reveals that lattice fringes with an interplanar spacing of 0.35 nm that matches the (002) plane of the monoclinic $CoMoO_4$ phase[44] as well as lattice fringes with a lattice spacing of 0.24 nm corresponding to the (311) plane of Co_3O_4.[14] The elemental composition of $CoMoO_4@Co_3O_4$ is determined by EDS and the elemental maps (Fig. 5(f)–(i)) indicate uniform distributions of cobalt, oxygen, and molybdenum on the particles.

3.2 Electrochemical characterization

By altering the hydrothermal synthesis formula and process while keeping the other parameters the same, the surface coverage, amount of coated active materials, and electrical characteristics of the samples are evaluated. Cyclic voltammetry (CV) and chronopotentiometry are conducted to determine the specific capacitance and electrochemical properties of the electrodes. Fig. 6(a) discloses that the capacitance of the $CoMoO_4@Co_3O_4$ fabricated on the nickel covered silicon is negligible, whereas $CoMoO_4@Co_3O_4$/OMEP shows considerably larger capacitance because of the larger enclosed area in the CV curve [Fig. 6(a), 20 mV s^{-1}] and longer discharge time [Fig. 6(b), 8 mA cm^{-2} charging–discharging current] than the OMEP, Co_3O_4, or $CoMoO_4$ fabricated on the OMEP and $CoMoO_4@Co_3O_4$ on nickel. Furthermore, as shown in Fig. 6(a), Co_3O_4/OMEP shows a similar enclosed area as $CoMoO_4$/OMEP but smaller area than $CoMoO_4@Co_3O_4$/OMEP because $CoMoO_4@Co_3O_4$/OMEP has more abundant nanomaterials and the composite structure improves the performance of the electrode.

Consistent with CV, at the current density of 8 mA cm^{-2}, the discharge time of the OMEP (22.82 s) is negligible and meanwhile, Co_3O_4/OMEP and $CoMoO_4$/OMEP show a short discharge time of 121 s and 108 s and a coulombic efficiency (CE) of 58.36% and 85.13%, respectively. As expected, $CoMoO_4@Co_3O_4$/OMEP shows a longer discharge time of 343 s and a CE of 69.3% because the nanostructured $CoMoO_4$ has an excellent ion transport capacity that promotes the activity of Co_3O_4 that adheres well onto the $CoMoO_4$ surface.

The CV curves obtained at various scanning rates from $CoMoO_4@Co_3O_4$/OMEP are displayed in Fig. 6(c) and those of Co_3O_4/OMEP and $CoMoO_4$/OMEP are presented in Fig. S5(a) and (c)† for comparison. As the scanning rate is increased from 10 to 150 mV s^{-1}, the peak current increase gradually. The oxidation and reduction peaks are apparent and peak shape is similar, especially at scanning rates below 80 mV s^{-1}. However, the peak potential shifts to the anodic and cathodic directions, respectively, because of more substantial polarization at larger scanning rates. As the scanning rate is increased, the peak currents are proportional to the square root of the scanning rates, implying that the electrodes have good electrochemical

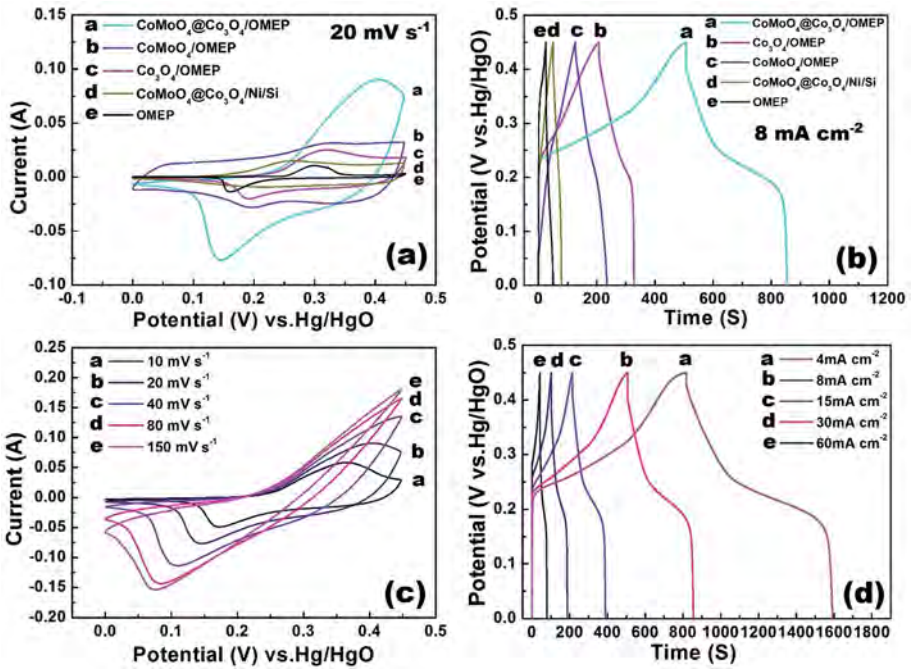

Fig. 6 (a) Cyclic voltammetry curves at the scanning rate of 20 mV S^{-1} and (b) 8 mA cm^{-2} charge–discharge curves of the newly fabricated OMEP, $CoMoO_4@Co_3O_4$/OMEP, $CoMoO_4$/OMEP, Co_3O_4/OMEP and $CoMoO_4@Co_3O_4$/Ni/Si electrode; (c) CV curves of $CoMoO_4@Co_3O_4$/OMEP at different scanning rates and (d) charging–discharging curves of $CoMoO_4@Co_3O_4$/OMEP at different current densities after activation.

performance. In the CV curve, there is a small angle along the horizontal axis indicating that the electrodes have smaller impedance. The combination of the probable chemical reactions from Co_3O_4 and $CoMoO_4$ is listed as follows:[6,45,46]

$$Co_3O_4 + OH^- + H_2O \leftrightarrow 3CoOOH + e^- \quad (6)$$

$$CoOOH + OH^- \leftrightarrow CoO_2 + H_2O + e^- \quad (7)$$

$$3[Co(OH)_3]^- \leftrightarrow Co_3O_4 + 4H_2O + OH^- + 2e^- \quad (8)$$

The two pairs of visible redox peaks in the CV curves confirm reactions (6)–(8), suggesting that instead of a pure electrical double-layer capacitance, the measured faradaic electrochemical electrode is dominated by a redox mechanism. It should be emphasized that the anodic peak potential, CV change, and cathodic peak potential shift in the anodic and cathodic directions with increasing sweeping rates decrease the capacitance. At a large scanning rate, unlike the CV from $CoMoO_4@Co_3O_4$/OMEP, the CV from Co_3O_4/OMEP and $CoMoO_4$/OMEP shows a faster current response indicating that $CoMoO_4@Co_3O_4$/OMEP has more materials participate in the reaction and part of materials do not respond adequately at high scanning rates.

To evaluate the potential application of the 3D OMEP comprising the nanostructured electrode ($CoMoO_4@Co_3O_4$/OMEP), the chronopotentiometry characteristics are evaluated at current densities from 4 to 60 mA cm^{-2}. According to the chronopotentiometric results in Fig. 6(d), the total active mass loading of 6.1 mg cm^{-2} and formula (1) and (2), the area (specific) capacitance values are calculated to be 7.13, 6.25, 5.88, 5.75, and 5.21 F cm^{-2} (1168.0, 1024.6, 914.75 and 854.1 F g^{-1}) for discharge current densities of 4, 8, 15, 30 and 60 mA cm^{-2}, respectively. The capacitances obtained from $CoMoO_4@Co_3O_4$/OMEP are much larger than those from the $Co_3O_4@NiCo_2O_4$ core–shell structure (2.94 F cm^{-2} at a discharge current density of 3 mA cm^{-2}) described by Xu *et al.*[45] The $CoMoO_4@NiMoO_4$ core–shell nanosheet arrays on nickel foam (2.22 F g^{-1} and 1106.9 F g^{-1} at a discharge current of 60 mA cm^{-2}) reported by Zhang *et al.*[44] and the specific capacitance is comparable to those obtained from the forest-like $Co_3O_4@CoMoO_4$ core–shell electrode (1200 F g^{-1} at a discharge current of 10 A g^{-1}) prepared by Wang *et al.*[35] and $NiCo_2O_4@MnMoO_4$ electrodes (1252.6 F g^{-1} at 20 mA cm^{-2}) by Cui *et al.*[27] The chronopotentiometry curves of $CoMoO_4$/OMEP and Co_3O_4/OMEP are shown in Fig. S5(b) and (d).† The comparison of the interfacial capacitances calculated with and formula (2) and (3) from CV and chronopotentiometry curves of the $CoMoO_4$/OMEP, Co_3O_4/OMEP electrodes at different scanning rates and current density is presented in Fig. S6(a) and (b)† respectively. All the tests show that the OMEP and $CoMoO_4@Co_3O_4$ composite improves the device performance.

Long-time performance tests are carried out to evaluate the stability of the samples and the results are shown in Fig. 7(a).

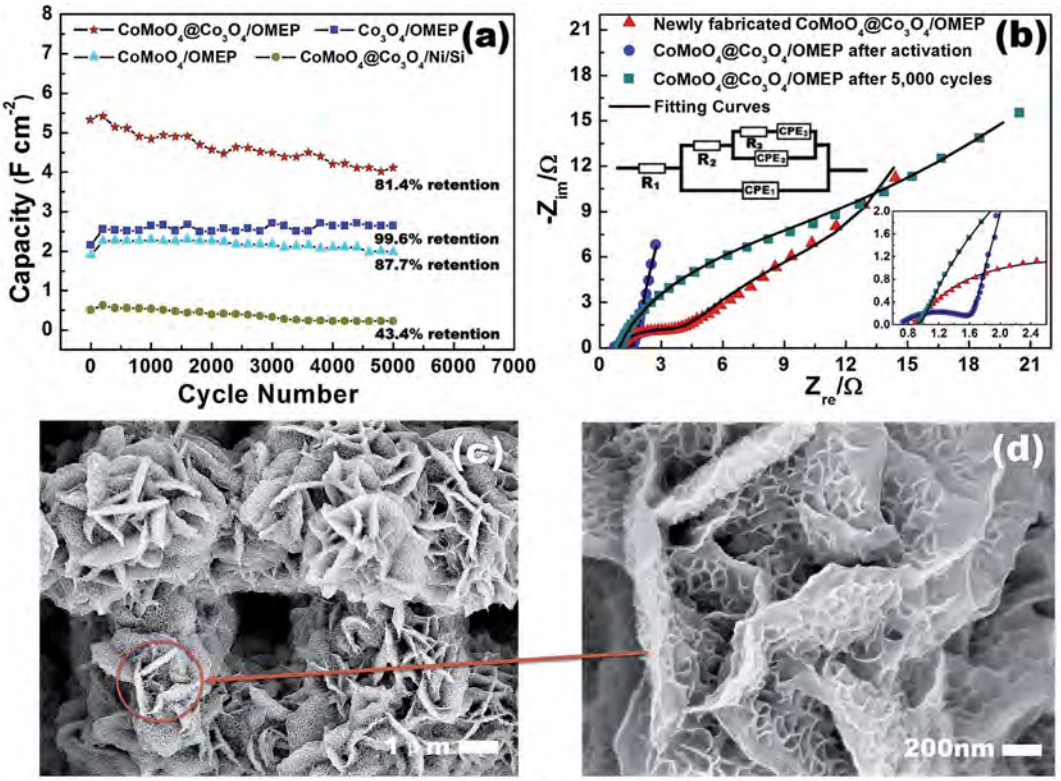

Fig. 7 (a) Long-term performance of the $CoMoO_4@Co_3O_4$/OMEP assessed at a charging–discharging current density of 100 mA cm^{-2}; (b) Nyquist plots of the newly fabricated $CoMoO_4@Co_3O_4$/OMEP electrode and that after activation and after 5000 cycles in the long-term performance test in a 2 M KOH solution with the equivalent circuit; (c) morphological characteristics of $CoMoO_4@Co_3O_4$/OMEP composite after 5000 cycles; (d) partial amplification view of (c).

The $CoMoO_4$@Co_3O_4/Ni/Si shows a 56.6% sharp capacitance drop probably due to the smooth structure of nickel deposited on the 2D silicon wafer against the firm bonding of $CoMoO_4$@Co_3O_4 during the Faraday reaction. The capacitances of $CoMoO_4$/OMEP and Co_3O_4/OMEP are stable with a capacitance retention of 87.7% and 99.6% after 5000 cycles at a current density of 100 mA cm^{-2}, respectively. The capacity stability observed from the two samples may arise from single nanoparticles with less active sites on the surface that can be closely connected with the substrate and undergo continuous electrochemical reactions. While the capacitance of $CoMoO_4$@Co_3O_4/OMEP shows 81.4% retention because of the largest amount of composite active materials in the OMEP pores and close integration with OMEP, during the reaction, the composite may undergo some transformation and reconstruction reducing the capacity. The reconstruction may originate from the reaction of $CoMoO_4$ and Co_3O_4 under alkaline conditions and Co^{2+} ions in the solution are re-grown on the surface of the $CoMoO_4$ nanoflakes electrochemically. The surface structure of $CoMoO_4$@Co_3O_4/OMEP after 5000 cycles is shown in Fig. 7(c) and (d). At the same time, the SEM in Fig. 7 and S3(c)† show that the structure has not been damaged after a series of tests in KOH, because the nickel layer deposited on Si-MCP by the liquid flow plating method is thick enough to prevent the silicon substrate from corrosion.

EIS is performed on the $CoMoO_4$@Co_3O_4/OMEP electrodes with an AC perturbation of 5 mV from 0.01 Hz to 100 000 Hz. Fig. 7(b) shows the EIS data obtained at three different stages, the newly fabricated electrode, after activation, and after 5000 cycles. The equivalent circuit and results in the inset are fitted to the impedance spectra.[47] The electrode internal resistance R_1 is less than 1 Ω indicating a highly conductive nature. The faradaic charge transfer resistance (R_2) corresponding to the semicircle in the high frequency range is associated with the surface properties of the electrode. In the equivalent circuit, we introduce the constant phase element (CPE) component.[47] CPE_1 and CPE_2 represent the double-layer and faradaic capacitance that vary with frequencies. This pure capacitance behavior can be explained by the distribution effects[48] and porosity[49] of the samples. On account of the influence of the 3D structure of the OMEP on mass transport, CPE_3 represents the Warburg impedance.[50]

Table 1 shows that the newly fabricated sample has an R_2 value of 3.450 Ω. After the activation process, it is 1.024 Ω and after 5000 cycles, it is 4.930 Ω, which is consistent with the double-layer capacitance CPE_{1-n} of $CoMoO_4$@Co_3O_4/OMEP (0.698 Ω) after activation (0.525 Ω) and after 5000 cycles (0.545 Ω). $CoMoO_4$@Co_3O_4/OMEP after activation yields a larger double layer capacitance which may be due to the fact that the active materials on the sample have more contact with the electrolyte. Most of the nanostructure recombines or adsorb/desorb ions and after cycling, some of the active materials drop from the substrate. The capacitance is a pseudo one and so the parameters R_3 and CPE_{2-n} are the key performance indicators. The R_3 values before, after activation, and after cycling are 30.2 Ω, 0.82 Ω and 9.802 Ω, respectively, because the active materials react more with the electrolyte. Most of the nanostructure is activated and more active substances take part in the reaction. Comparison of CPE_{2-n} shows that the newly made sample has a CPE_{2-n} of 0.652 that is smaller than that after activation of 1.016 and after cycling of 4.811.[51] Furthermore, the slope of the impedance plots (CPE_{3-n}) is 0.831 after activation and 0.809 after cycling compared to 0.649 of the newly fabricated sample at low frequencies. This indicates that the special complex microstructure with flakes and sheets enables faster ion diffusion through the channels of the OMEP but after 5000 cycles, some of the structure collapses.

Table 1 Important fitted parameters for the equivalent circuit

	R_1	R_2	R_3	CPE_{1-n}[a]	CPE_{2-n}	CPE_{3-n}
Initial	0.880	3.450	30.20	0.698	0.652	0.649
After activation	0.690	1.024	0.820	0.525	1.016	0.831
After 5000 cycles	0.868	4.930	9.802	0.545	4.811	0.809

[a] CPE-n represents the exponential parameter of constant phase element.

3.3 Electrochemical properties of the $CoMoO_4$@Co_3O_4 hybrid device

To further evaluate the commercial potential of $CoMoO_4$@Co_3O_4, a hybrid device composed of the $CoMoO_4$@Co_3O_4/OMEP electrode as the anode, activated carbon and conductive carbon black on nickel foam as the cathode in a quasi-solid electrolyte together with one piece of PE membrane as the separator is prepared. They are packaged by a CR2025 standard battery cell.[36] The oxidation and reduction peaks can be observed from Fig. 8(a) and the peak current becomes larger as the scanning rate is increased from 10 to 400 mV s^{-1}. However, there is no obvious distortion in the CV curve even at a scanning rate of 400 mV s^{-1}, corroborating the large comparative area and rapid ion diffusion capability of the composite nanostructures on the OMEP resulting in the fast charging–discharging properties of the device.[52] Fig. S7(a)† shows that the potential window of the $CoMoO_4$@Co_3O_4/OMEP electrode is 0 to 0.45 V. On the other hand, there is a rectangular CV curve from −1.1 to 0 V for the AC electrode, indicative of the EDLC behavior. Therefore, the total cell voltage of the ASC device can be increased up to 1.5 V, which is the sum of the potential range for the AC and $CoMoO_4$@Co_3O_4/OMEP electrodes.[44]

The charging–discharging test is performed at various current densities. As shown in Fig. 8(b), the shape of the charging–discharging curves at different current densities resembles a triangle and the discharge curves show a good discharge platform at around 1.3 V, suggesting rapid I–V response and good electrochemical reversibility. The relationship between the specific capacitance and current density during charging–discharging is shown in Fig. S7(b)† which shows that the capacitance of the device is up to 149.01 F g^{-1} at a current of 2 A g^{-1}. The performance of our device is better than that of $CoMoO_4$@Co_3O_4 NPF//CNTs ASC (128 F g^{-1} at 3 A g^{-1}),[35] NF–Co_2AlO_4@MnO_2//NF–Fe_3O_4 (99.13 F g^{-1} at 1 A g^{-1}),[53]

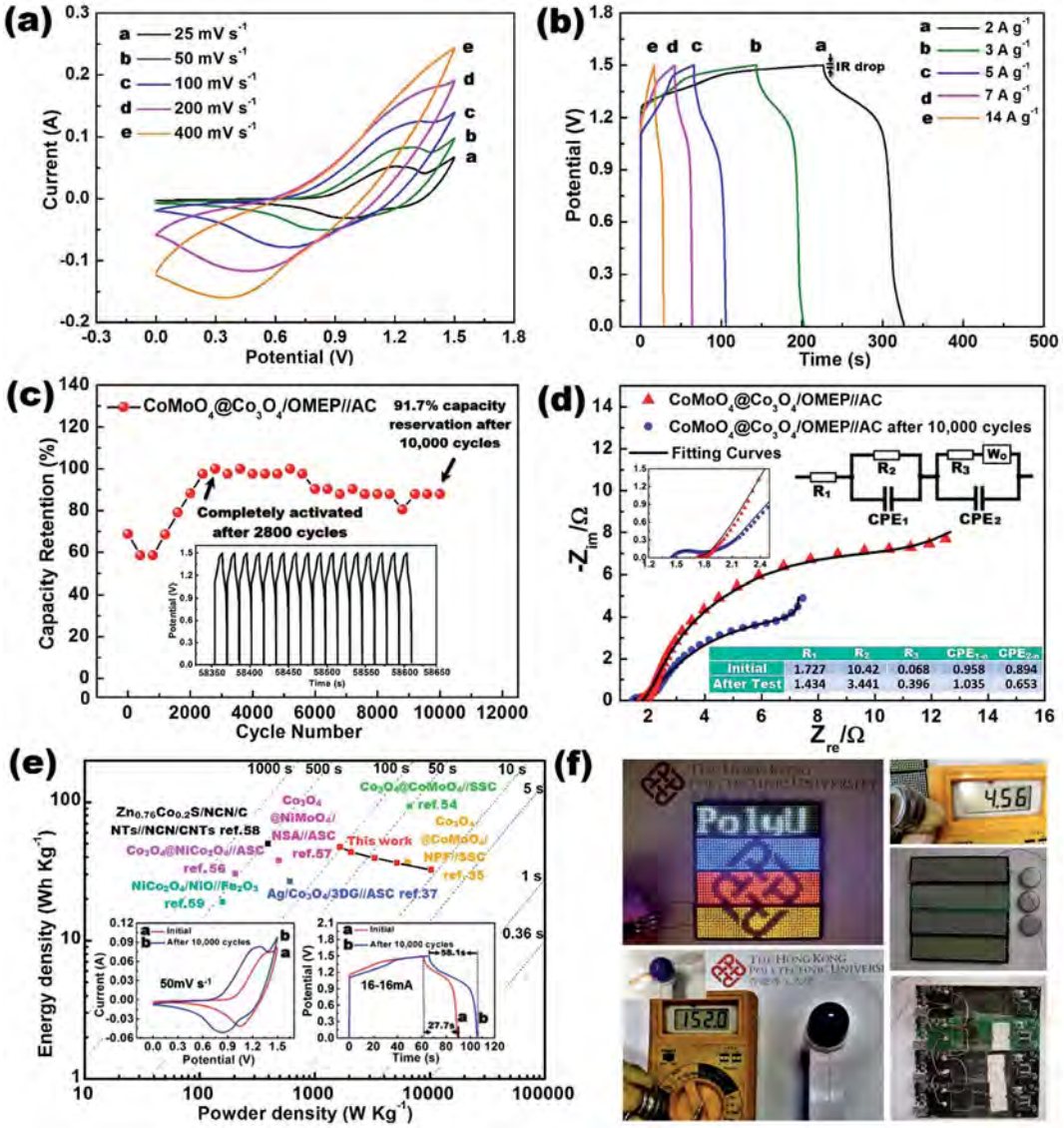

Fig. 8 (a) CVs acquired at different scanning rates between 0 and 1.5 V; (b) charging–discharging curves of the asymmetric supercapacitor at different current densities; (c) cycling stability of the 10 000 cycles of device at large current densities and cycle curve in the intermediate stage; (d) Nyquist plots of the as-assembled ASC before and after 10 000 cycles in the long-term performance test with the equivalent circuit and elements fitting the impedance curve; (e) Ragone plot of the as-assembled ASC (insets is the comparison of CV and IT curves from the as-assembled ASC before and after 10 000 cycles); (f) four parallel programmed LED arrays and a commercial fan motor powered by the three parallel as-assembled ASCs, 4.56 V voltage window by a voltmeter, the as-assembled ASCs, and positive and negative sides of the LED arrays.

and $NiCo_2S_4$@$Co(OH)_2$//AC (100.94 F g^{-1} at 0.5 A g^{-1})[26] and comparable to that of NMO-NS//AC ASC (151.7 F g^{-1} at 1 A g^{-1})[15] and Co_3O_4@$CoMoO_4$//Co_3O_4@$CoMoO_4$ (148.4 F g^{-1} at 0.5 A g^{-1}).[37] Fig. 8(c) reveals the outstanding cycling life of the device up to 10 000 times at a large charging–discharging current of 100 mA, which has rarely been demonstrated from quasi-solid electrolyte based hybrid devices. Because of the activation process, the cycling capability of the hybrid device is completely activated and improved dramatically in the first 2800 cycles (100% capacitance after 2800 cycles). When approaching 5800 cycles at a large current, the capacitance exhibits an 8.1% loss and after this attenuation, the capacitance stabilizes in the following 2400 cycles. The cycling ability of our device under a large current density is better than that of most devices shown in Table 2.

To explain the significant attenuation of the hybrid device with cycles, EIS is performed. The Nyquist plots of the newly fabricate ASC device and 10 000th charge–discharge cycles, the corresponding equivalent circuits and fitting parameters are presented in Fig. 8(d) and can be analyzed as follows. The spectra at frequencies above 2 kHz are dominated by connections including external cell connections, electronic conduction between the substrate and active materials, and ionic conduction through the electrolyte. In our circuit model, the resistor R_0 is used to simulate the pure resistive behavior. The semicircle between 2 kHz and 50 Hz is related to the solid electrolyte

Table 2 Comparison of the as-assembled ASC with those reported in the literature

Electrode composition	Electrolyte	Specific capacitance ($F\ cm^{-2}$ or $F\ g^{-1}$)	Voltage HI limit (V)	Maximum energy density ($W\ h\ kg^{-1}$)	Maximum power density ($kW\ kg^{-1}$)	Cyclic ability (retention)	Ref.
Co_3O_4@$NiCo_2O_4$||JF-2	KOH solution	Or 430	1.6	42.5	0.1	97% after 7000 cycles	56
Co_3O_4@$NiMoO_4$||AC	KOH solution	2.67 or 1526	1.5	25.3	4.82	70% after 1000 cycles	57
Co_3O_4@$CoMoO_4$||Co_3O_4@$CoMoO_4$	KOH solution	Or 1040	1.6	92.44	6.55	91.% after 5000 cycles	54
Co_3O_4@$CoMoO_4$ NPF||CNTs	KOH solution	6.27 or 1902	1.6	37.0	6.4	98.5% after 3000 cycles	35
Ag/Co_3O_4/3DG||AC	KOH solution	0.421 or 1052.5	1.5	26.7	0.60	91.6% after 10 000 cycles	37
$Zn_{0.76}Co_{0.24}S$/NGN/CNTs||NGN/CNTs	KOH solution	Or 1482	1.5	50.2	0.39	100% after 2000 cycles	58
$NiCo_2O_4$/NiO||Fe_2O_3	KOH solution	Or 955	1.3	19	0.16	97% after 5000 cycles	59
$CoMoO_4$@Co_3O_4/OMEP||AC	KOH solution	7.13 or 1168.0	1.5	32.4	10.3	91.7% after 10 000 cycles	This work

interface (SEI) layer which can be simulated by a resistor R_1 in parallel with a constant phase-angle element (CPE) named CPE_1. The impedance between 50 Hz and 0.01 Hz can be attributed to the charge transfer and diffusion of OH^- ions from the reaction interface to the bulk of the porous of the OMEP. Another CPE named CPE_2 in parallel with resistor R_2 is employed to simulate the charge transfer behavior. Finally, a Warburg impedance W_0 is used to simulate the behavior of diffusion of OH^- ions.

According to the table in Fig. 8(d), the contact resistance R_1 of the sample after 10 000 cycles is 1.434 Ω which is smaller than that of the initial sample (1.727 Ω) because active substances participate more in the chemical reactions that reduce the contact resistance. In addition, resistance R_2 associated with the SEI layer of the sample after 10 000 cycles is 3.44 Ω which is smaller than that of the initial sample (10.42 Ω) perhaps due to more contact between the active substance and electrolyte. R_3 for the circular arc diameter after the test is larger than that of the initial sample. It can be attributed to the gradual damage of the Ni coating and structure of $CoMoO_4$@-Co_3O_4/OMEP with time and increasing difficulty for OH^- diffusion from the reaction interface to the bulk of the OMEP.

The energy and power densities of the $CoMoO_4$@Co_3O_4/OMEP in the assembled ASC are calculated according to the equation described as formula (4) and (5) and shown in Fig. 8(e). In addition, literature values of Co-based ternary oxides are given for comparison in Fig. 8(e) and Table 2. The total mass of the active material of $CoMoO_4$@Co_3O_4 and discharge time are considered in the calculation of energy and power densities. The ASC delivers a maximum energy density of 45.98 W h kg^{-1} at power density of 1647.5 W kg^{-1} and even at 10 245.6 W kg^{-1}, the device still shows an energy density of 32.359 W h kg^{-1}. As mentioned above, this is one of the best values reported from the ASC configuration irrespective of the positive or negative electrodes. For instance, it is better than $CoMoO_4$@$NiMoO_4$/Ni foam//AC (28.7 W h kg^{-1} at 267 W kg^{-1}),[44] $CoMoO_4$@Co_3O_4 NPF//CNTs (37.0 W h kg^{-1} at 6400 W kg^{-1}),[35] and Co_3O_4@$NiMoO_4$//AC (25.3 W h kg^{-1} at 482 W kg^{-1})[57] and comparable to Co_3O_4@$CoMoO_4$//Co_3O_4@$CoMoO_4$ (92.44 W h kg^{-1} at 6550 W kg^{-1})[54] and $CoMoO_4$@$NiMoO_4 \cdot xH_2O$//Fe_2O_3 (26.7 W h kg^{-1} at 12 000 W kg^{-1}).[55] The excellent electrochemical performance of the $CoMoO_4$@Co_3O_4/OMEP electrode and as-assembled ASC can be attributed to the composite nanostructure growing evenly on the surface and side wall of the three-dimensional OMEP substrate thus avoiding agglomeration of the nanomaterials, improving the ion transport efficiency between the nanomaterials and electrolytes, enhancing the cycling ability, and delivering large energy and power densities.

As shown in Fig. 8(f), the three as-assembled ASCs in parallel after charging each device with a large current about 10 s can power four parallel programmable LED arrays efficiently. The LED array as shown in the positive and negative sides in Fig. 8(f) is made up of 1936 small LEDs (11 × 44 × 4) and programmable chips with functional circuits that can be designed by computer. The commercial fan motor is also powered efficiently by the three paralleled as-assembled ASCs at a current density of

0.152 A and voltage of 4.56 V, thus illustrating that our device has good supercapacitive characteristics and large commercial potential in high-performance energy storage systems.

4. Conclusion

The $CoMoO_4@Co_3O_4$ nanocomposite produced uniformly on a 3D OMEP hydrothermally allows synergistic contributions from the active materials and substrate giving rise to better electrochemical performance. $CoMoO_4@Co_3O_4$/OMEP has a large specific capacitance of 7.13 F cm^{-2} (1168.0 F g^{-1}) at a constant current density of 0.6 A g^{-1} and a retention of 81.4% after 5000 cycles. The hybrid device composed of the $CoMoO_4@Co_3O_4$/OMEP//AC delivers large specific energy densities at different power densities as well as superior cycling stability. The hierarchical $CoMoO_4@Co_3O_4$ nanocomposite is promising and bridges the gap between traditional energy storage and power generation device.

Acknowledgements

This research was supported by the Postdoctoral Fellowships Scheme and the research funding from Research Institute for Sustainable Urban Development, The Hong Kong Polytechnic University. The work was also financially sponsored by City University of Hong Kong Applied Research Grant (ARG) No. 9667122 and Strategic Research Grant (SRG) No. 7004644.

References

1 P. Simon and Y. Gogotsi, *Nat. Mater.*, 2008, **7**, 845–854.
2 H. M. Lee, S. W. Cho, C. J. Song, H. J. Kang, B. J. Kwon and C.-K. Kim, *Electrochim. Acta*, 2015, **160**, 50–56.
3 H. Chuo, H. Gao, Q. Yang, N. Zhang, W. Bu and X. Zhang, *J. Mater. Chem. A*, 2014, **2**, 20462–20469.
4 H. Huang, C. Lei, G. Luo, Z. Cheng, G. Li, S. Tang and Y. Du, *J. Mater. Sci.*, 2016, **51**, 6348–6356.
5 Z. Gao, C. Bumgardner, N. Song, Y. Zhang, J. Li and X. Li, *Nat. Commun.*, 2016, **7**, 11586.
6 T. Deng, W. Zhang, O. Arcelus, J. G. Kim, J. Carrasco, S. J. Yoo, W. Zheng, J. Wang, H. Tian and H. Zhang, *Nat. Commun.*, 2017, **8**, 15194.
7 J. Zhi, O. Reiser and F. Huang, *ACS Appl. Mater. Interfaces*, 2016, **8**, 8452–8459.
8 H. G. Wang, D. L. Ma, Y. Huang and X. B. Zhang, *Chem.–Eur. J.*, 2012, **18**, 8987–8993.
9 M. Chen, J. Liu, D. Chao, J. Wang, J. Yin, J. Lin, H. Jin Fan and Z. Xiang Shen, *Nano Energy*, 2014, **9**, 364–372.
10 Y. Wang, T. Zhou, K. Jiang, P. Da, Z. Peng, J. Tang, B. Kong, W.-B. Cai, Z. Yang and G. Zheng, *Adv. Energy Mater.*, 2014, **4**, 1400696.
11 Y. Zuo, J. J. Ni, J. M. Song, H. L. Niu, C. J. Mao, S. Y. Zhang and Y. H. Shen, *Appl. Surf. Sci.*, 2016, **370**, 528–535.
12 D. Cai, D. Wang, B. Liu, L. Wang, Y. Liu, H. Li, Y. Wang, Q. Li and T. Wang, *ACS Appl. Mater. Interfaces*, 2014, **6**, 5050–5055.
13 H. Pang, X. Li, Q. Zhao, H. Xue, W. Y. Lai, Z. Hu and W. Huang, *Nano Energy*, 2017, **35**, 138–145.
14 L. Bao, T. Li, S. Chen, C. Peng, L. Li, Q. Xu, Y. Chen, E. Ou and W. Xu, *Small*, 2017, **13**, 1602077.
15 R. Rakhi, W. Chen, D. Cha and H. N. Alshareef, *Nano Lett.*, 2012, **12**, 2559–2567.
16 S. Farhadi, K. Pourzare and S. Sadeghinejad, *Polyhedron*, 2014, **67**, 104–110.
17 Z. Wei, J. Wang, S. Mao, D. Su, H. Jin, Y. Wang, F. Xu, H. Li and Y. Wang, *ACS Catal.*, 2015, **5**, 4783–4789.
18 X. H. Xia, J. P. Tu, X. L. Wang, C. D. Gu and X. B. Zhao, *Chem. Commun.*, 2011, **47**, 5786–5788.
19 Y. Liang, Y. Li, H. Wang, J. Zhou, J. Wang, T. Regier and H. Dai, *Nat. Mater.*, 2011, **10**, 780–786.
20 P. Poizot, S. Laruelle, S. Grugeon, L. Dupont and J. M. Tarascon, *Nature*, 2000, **407**, 496–499.
21 P. Yang, X. Xiao, Y. Li, Y. Ding, P. Qiang, X. Tan, W. Mai, Z. Lin, W. Wu and T. Li, *ACS Nano*, 2013, **7**, 2617–2626.
22 L. Q. Mai, F. Yang, Y. L. Zhao, X. Xu, L. Xu and Y.-Z. Luo, *Nat. Commun.*, 2011, **2**, 381.
23 Q. Ke, C. Guan, X. Zhang, M. Zheng, Y. W. Zhang, Y. Cai, H. Zhang and J. Wang, *Adv. Mater.*, 2017, **29**, 1604164.
24 L. Huang, W. Zhang, J. Xiang, H. Xu, G. Li and Y. Huang, *Sci. Rep.*, 2016, **6**, 31465.
25 X. Li, S.-Y. Lin, M. Zhang, G. Jiang and H. Gao, *Nano*, 2016, **11**, 1650050.
26 R. Li, S. Wang, Z. Huang, F. Lu and T. He, *J. Power Sources*, 2016, **312**, 156–164.
27 C. Cui, J. Xu, L. Wang, D. Guo, M. Mao, J. Ma and T. Wang, *ACS Appl. Mater. Interfaces*, 2016, **8**, 8568–8575.
28 A. Vu, Y. Qian and A. Stein, *Adv. Energy Mater.*, 2012, **2**, 1056.
29 M. Li, S. Xu, T. Liu, F. Wang, P. Yang, L. Wang and P. K. Chu, *J. Mater. Chem. A*, 2013, **1**, 532–540.
30 Y. Wang, Z. Zhong, Y. Chen, C. T. Ng and J. Lin, *Nano Res.*, 2011, **4**, 695.
31 D. Yuan, P. Ci, F. Tian, J. Shi, S. Xu, P. Xin, L. Wang and P. K. Chu, *J. Micro/Nanolithogr., MEMS, MOEMS*, 2009, **8**, 033012–033017.
32 C. Liang, L. L. Chen, D. J. Wu, C. Zhang, S. H. Xu, Y. P. Zhu, D. Y. Xiong, P. X. Yang, L. W. Wang and P. K. Chu, *Mater. Lett.*, 2016, **172**, 40–43.
33 S. Furukawa and M. Mehregany, *Sens. Actuators, A*, 1996, **56**, 261–266.
34 D. Wu, S. Xu, C. Zhang, Y. Zhu, D. Xiong, R. Huang, R. Qi, L. Wang and P. K. Chu, *J. Mater. Chem. A*, 2016, **4**, 11317–11329.
35 J. Wang, X. Zhang, Q. Wei, H. Lv, Y. Tian, Z. Tong, X. Liu, J. Hao, H. Qu and J. Zhao, *Nano Energy*, 2016, **19**, 222–233.
36 M. Li, S. Xu, C. Cherry, Y. Zhu, R. Huang, R. Qi, P. Yang, L. Wang and P. K. Chu, *Electrochim. Acta*, 2014, **149**, 18–27.
37 J. Wang, W. Dou, X. Zhang, W. Han, X. Mu, Y. Zhang, X. Zhao, Y. Chen, Z. Yang and Q. Su, *Electrochim. Acta*, 2017, **224**, 260–268.
38 M. Li, S. Xu, C. Cherry, Y. Zhu, D. Wu, C. Zhang, X. Zhang, R. Huang, R. Qi and L. Wang, *J. Mater. Chem. A*, 2015, **3**, 13776–13785.
39 V. V. Atuchin, O. Y. Khyzhun, O. D. Chimitova, M. S. Molokeev, T. A. Gavrilova, B. G. Bazarov and J. G. Bazarova, *J. Phys. Chem. Solids*, 2015, **77**, 101–108.

40 M. J. Barmi and M. Minakshi, *Chempluschem*, 2016, **81**, 964–977.
41 X. Tong, D. Wu, C. Zhang, K. Lian, D. Xiong, S. Xu, Y. Zhu, R. Qi, R. Huang and L. Wang, *J. Mater. Chem. A*, 2017, **6**, 2629–2639.
42 B. Cao, G. M. Veith, J. C. Neuefeind, R. R. Adzic and P. G. Khalifah, *J. Am. Chem. Soc.*, 2013, **135**, 19186–19192.
43 X. W. Wang, D. L. Zheng, P. Z. Yang, X. E. Wang, Q. Q. Zhu, P. F. Ma and L. Y. Sun, *Chem. Phys. Lett.*, 2017, **667**, 260–266.
44 Z. Zhang, H. Zhang, X. Zhang, D. Yu, Y. Ji, Q. Sun, Y. Wang and X. Liu, *J. Mater. Chem. A*, 2016, **4**, 18578–18584.
45 X. Wu, Z. Han, X. Zheng, S. Yao, X. Yang and T. Zhai, *Nano Energy*, 2017, **31**, 410–417.
46 X. Yu, B. Lu and Z. Xu, *Adv. Mater.*, 2014, **26**, 1044.
47 G. Barral, F. Njanjo-Eyoke and S. Maximovitch, *Electrochim. Acta*, 1995, **40**, 2815–2828.
48 G. Brug, A. Van Den Eeden, M. Sluyters-Rehbach and J. Sluyters, *J. Electroanal. Chem. Interfacial Electrochem.*, 1984, **176**, 275–295.
49 L. Gassa, J. Vilche, M. Ebert, K. Jüttner and W. Lorenz, *J. Appl. Electrochem.*, 1990, **20**, 677–685.
50 M. E. Orazem and B. Tribollet, *Electrochemical Impedance Spectroscopy*, John Wiley & Sons, 2011.
51 B. E. Conway, *Electrochemical Supercapacitors: Scientific Fundamentals and Technological Applications*, Springer, 1999.
52 Y.-M. Wang, X. Zhang, C.-Y. Guo, Y.-Q. Zhao, C.-L. Xu and H.-L. Li, *J. Mater. Chem. A*, 2013, **1**, 13290–13300.
53 F. Li, H. Chen, X. Y. Liu, S. J. Zhu, J. Q. Jia, C. H. Xu, F. Dong, Z. Q. Wen and Y. X. Zhang, *J. Mater. Chem. A*, 2016, **4**, 2096–2104.
54 Z. Gu, R. Wang, H. Nan, B. Geng and X. Zhang, *J. Mater. Chem. A*, 2015, **3**, 14578–14584.
55 J. Wang, L. Zhang, X. Liu, X. Zhang, Y. Tian, X. Liu, J. Zhao and Y. Li, *Sci. Rep.*, 2017, **7**, 41088.
56 P. Sennu, V. Aravindan and Y. S. Lee, *J. Power Sources*, 2016, **306**, 248–257.
57 W. Hong, J. Wang, P. Gong, J. Sun, L. Niu, Z. Yang, Z. Wang and S. Yang, *J. Power Sources*, 2014, **270**, 516–525.
58 H. Tong, W. Bai, S. Yue, Z. Gao, L. Lu, L. Shen, S. Dong, J. Zhu, J. He and X. Zhang, *J. Mater. Chem. A*, 2016, **4**, 11256–11263.
59 A. Shanmugavani and R. K. Selvan, *Electrochim. Acta*, 2016, **189**, 283–294.